Catalysis Today 145 (2009) 243–250

Contents lists available at ScienceDirect

Catalysis Today

journal homepage: www.elsevier.com/locate/cattod

Carbon incorporation and deactivation of MgO(0 0 1) supported Pd nanoparticles during CO oxidation

P. Nolte [a], A. Stierle [a,*], O. Balmes [b], V. Srot [a], P.A. van Aken [a], L.P.H. Jeurgens [a], H. Dosch [a]

[a] Max-Planck-Institute for Metals Research, Heisenbergstr. 3, D-70569 Stuttgart, Germany
[b] European Synchrotron Radiation Facility, B. P. 220, 38043 Grenoble Cedex 9, France

ARTICLE INFO

Article history:
Available online 10 January 2009

Keywords:
CO oxidation
Pd
In situ XRD studies
TEM
XPS

ABSTRACT

We have investigated the structure and composition of the model catalyst system Pd/MgO(0 0 1) during oxidation, CO reduction and CO oxidation at near atmospheric pressures by a combination of in situ X-ray diffraction and ex situ transmission electron microscopy and spectroscopy techniques. From the in situ X-ray experiments, we find: (a) the Pd nanoparticles with 9 nm in diameter transform into epitaxial PdO above 10^{-1} mbar O_2 pressure at 570 K, (b) the oxidation process can be reverted by CO exposure, recovering Pd nanoparticles in their initial orientation, and (c) during CO oxidation in a mixture of 50 mbar O_2 and 50 mbar CO a new phase is evolving with lattice constant close to the MgO substrate value, which we assign to expanded Pd nanoparticles forming upon carbon incorporation. Ex situ transmission electron microscopy and different spectroscopy techniques uncover the CO_2 induced growth of a disordered overlayer containing C, Mg and O, which forms during CO oxidation and leads to an overgrowth of Pd nanoparticles thereby deactivating the catalyst.

1. Introduction

Palladium is a highly active catalyst used for a variety of industrially important chemical reactions, such as alkyne hydrogenation and methane oxidation [1,2]. In addition, it is an essential component of catalytic converters in automotive cars for oxidation or reduction of harmful exhaust gas components like CO and NO_x. These key applications of Pd have triggered an increasing demand for a detailed microscopic insight into its catalytic properties aiming to understand the involved chemical reactions at the atomic level, and ultimately, to develop tailor-made future catalysts with improved performance such as increased turnover frequencies, higher reaction selectivity and enhanced catalyst lifetime.

In the case of oxidation reactions, it is generically unclear, whether chemisorbed oxygen or ultrathin "surface oxide" phases [3] or PdO bulk oxide is the catalytically most active phase. The reaction mechanism is in the first case described by a Langmuir–Hinshelwood and in the second case by a Mars–van-Krevelen reaction mechanism [4–6]. In particular, CO oxidation was studied on well-defined model systems both by experiment and theory, ranging from Pd single crystal and stepped (vicinal) surfaces to Pd nanoparticles on epitaxial ultrathin film oxide supports. Several in situ studies of Pd(1 0 0) have been carried out at atmospheric pressures: scanning tunneling microscopy (STM) unraveled that the Pd(1 0 0) surface undergoes a pronounced roughening at 480 K when the CO_2 production rate was high [7,8], surface X-ray diffraction experiments during CO oxidation showed that a thin PdO bulk oxide layer is present during high catalytic activity [9]. From ab initio kinetic Monte–Carlo simulations it was concluded that an ultra-thin surface oxide layer is thermodynamically favored under reaction conditions [10]. On the other hand, from low pressure molecular beam experiments on Pd nanoparticles grown on epitaxial Fe_3O_4 films it was deduced that the partial oxidation of the Pd nanoparticles above 500 K leads to a reduced CO oxidation activity [11,12].

To shed new light on the relevant catalytic behavior of Pd nanoparticles and the role of the seemingly inert MgO support, we have performed an in situ surface X-ray diffraction study of MgO(0 0 1)-supported Pd nanoparticles during CO oxidation. The experiments have been carried out at 570 K near ambient pressures. Under oxygen exposure in the mbar pressure regime, the Pd nanoparticles convert to PdO nanoparticles epitaxially growing on the MgO substrate, exhibiting well-defined orientation relationships between the MgO and the PdO lattice. After CO reduction, Pd particles in original orientation and shape are recovered. We find that during CO oxidation, poorly ordered PdO islands are present, partially epitaxial to the MgO(0 0 1) substrate. Pd nanoparticles are observed to transform into a new phase with lattice spacing close to the MgO substrate, which we attribute to

* Corresponding author. Tel.: +49 711 6891842; fax: +49 711 6891902.
E-mail address: stierle@mf.mpg.de (A. Stierle).

0920-5861/$ – see front matter © 2008 Elsevier B.V. All rights reserved.
doi:10.1016/j.cattod.2008.12.002

carbon incorporation. During extended CO oxidation experiments, a surprising deactivation of the system was observed, which is related to the formation of a capping layer containing C, Mg and O, as revealed by ex situ investigation of the sample by a combination of structural and analytical tools (transmission electron microscopy (TEM), scanning transmission electron microscopy (STEM) with electron energy loss spectroscopy (EELS) and energy dispersive X-ray spectroscopy (EDXS), X-ray photoelectron spectroscopy (XPS) and Auger electron sputter depth profiling). Our results demonstrate that the extrapolation of reactivity experiments on Pd nanoparticles performed under UHV conditions does not allow a direct extrapolation to high pressure conditions, because new reaction pathways may be opened, which involve the MgO substrate.

2. Experimental details

A commercially available MgO(0 0 1) single crystal (misorientation $< 0.1^\circ$, 10 mm $\times$ 10 mm surface area, 1 mm thickness) was air annealed at 1400 °C for 1 h. After introduction to ultra high vacuum (UHV), it was sputtered at 1000 eV Ar ion energy for 1 h to remove Ca precipitates which arose from segregation during the high temperature air annealing. A small residual Ca signal was detected by Auger electron spectroscopy. Afterwards the substrate was annealed at a temperature of 920 K in an oxygen atmosphere at 5×10^{-6} mbar. 12 Pd monolayer equivalents (99.9% purity) were deposited at a substrate temperature of 670 K using a commercial e-beam evaporator leading to the growth of epitaxial Pd nanoparticles with about 30% size distribution [13]. After the deposition, the sample was transferred through air and it was subsequently inserted into the mobile high-pressure compatible UHV X-ray diffraction chamber [14]. The sample temperature was controlled by a chromel/alumel type K thermocouple attached to the sample (temperature accuracy $\pm$5 K). It was heated by an inert Al_2O_3 encapsulated heater. The pressure inside the chamber was controlled from UHV to atmospheric pressures by a combination of a cold cathode ion gauge and two capacitive high pressure gauges. The chamber was connected to an external gas manifold, allowing the preparation of defined CO/O_2 mixtures. Oxygen with 99.9995% and carbon monoxide with 99.997% purity were used. The CO was additionally cleaned by a Cu trap kept at 570 K to remove carbonyls. The chamber was run as a batch reactor (volume approximately 2 l), by backfilling it with the reactants and disconnecting to the vacuum pumps. The gas composition inside the chamber was monitored by leaking gas into a residual gas analyzer system. Prior to the X-ray diffraction experiment, a bake-out of the sample chamber was performed to obtain UHV conditions.

The X-ray experiment was carried out at beamline ID 03 at the European Synchrotron Radiation Facility in Grenoble, France. Monochromatic X-rays with photon energy of 14 keV were employed. The diffraction experiment was performed on a *z*-axis type surface diffractometer under grazing incidence (incident angle 0.16–0.17°, close to the critical angle of Pd for total external reflection). Throughout the paper, Pd reciprocal lattice coordinates are used with H and K in the surface plane and L perpendicular to the surface ($H(K, L) = 1$ corresponds to $2\pi/a_0$ with the Pd bulk lattice constant $a_0 = 389$ pm).

After the X-ray experiment two cross-sectional TEM specimens were prepared from part of the sample using the conventional cross-section method [15]. The specimens were subsequently sliced, grounded, polished and thinned by Ar-ion milling. Both specimens were carbon coated to avoid sample charging. TEM images were recorded using JEOL JEM 4000 FX and JEOL JEM 2000 FX electron microscopes at the Stuttgart Center for Electron Microscopy (StEM) at the MPI MF. Analytical TEM studies were carried out in a VG HB501UX dedicated STEM operated in ultra-high vacuum at an accelerating voltage of 100 keV. The spectra were acquired in spot mode with a beam diameter of 0.7 nm (full width at half maximum (FWHM)). The microscope has a cold field emission source and is equipped with an energy-dispersive X-ray spectrometer (EDXS) and an electron energy-loss spectrometer (EELS).

The depth-distributions of C, Pd, O and Mg were obtained after the in situ X-ray experiment by sputter-depth profiling using Auger electron spectroscopy (AES) [16]. To this end, spectra of the C-KLL, Pd-MNN, O-KLL and Mg-KLL Auger lines were recorded with a JEOL Jamp 7830F scanning Auger microscope (beam voltage of 3 keV; spot diameter $\sim$20 nm), while employing a discontinuous ion sputtering mode with 1-keV Ar^+ ions (at an incident angle of 55° with respect to the surface normal). The sputtered and analyzed areas were 300 μm $\times$ 300 μm and 10 μm $\times$ 10 μm, respectively. The sputter time was converted to an approximate sputter depth by adopting the known sputter rate of a Ta_2O_5 reference sample. Quantification was performed using the resolved peak-to-peak heights in the differentiated spectra and adopting the instrumental elemental sensitivity factors as provided by the manufacturer. Since the Pd-MNN and C-KLL lines have an overlap in the vicinity of 272 eV, the C contribution to the differentiated spectra was resolved in a two-step procedure. First a pure Pd reference spectrum was fitted to the measured Pd-MNN spectrum in the energy range of 300–350 eV by adopting a scaling factor and allowing small energy shifts of the pure Pd reference spectrum. Next, the accordingly scaled Pd contribution in the vicinity of the C-KLL line (around 272 eV) was subtracted from the measured C-KLL spectrum. The remaining signal was assigned the carbon KLL-signal.

Finally, the chemical composition of the sample surface was analyzed by X-ray photoelectron spectra (XPS) using a Thermo VG Thetaprobe system employing monochromatic Al Kα radiation (1486.68 eV; spot size 400 μm). XPS survey spectra were recorded with a step size of 0.2 eV at constant pass energy of 200 eV. Detailed spectra of the C 1s, Mg 1s, Pd 3d and combined O 1s–Pd 3p regions were recorded with a step size of 0.01 eV at a constant pass energy of 25 eV. Charge neutralization of the insulating sample during the XPS analysis was achieved by irradiation of the sample surface with a diffuse beam of low-energy electrons (kinetic energy of 0.5 eV; emission current 100 μA) combined with low-energy Ar^+ ions, as generated in a single mode of operation using a combined low-energy flood gun (Thermo Electron Type 822-06) filled with pure Ar gas at a constant pressure of about 5×10^{-4} mbar. Spectral decomposition of the as-measured spectra was performed by subtraction of a Shirley-type inelastic background over each energy region and subsequent, constrained, linear-least-squares fitting with one or more symmetric (mixed Gaussian–Lorentzian) peak components (while taking the same Gaussian–Lorentzian fraction and full-width-at-half maximum for similar components in the fitted spectrum).

3. In situ oxidation, CO reduction and CO oxidation experiments

Pd on MgO(0 0 1) grows in cube-on-cube epitaxy with a misfit of 8% to the MgO substrate ($a = 420$ pm) [17]. A minor part of the particles was observed to grow epitaxially with (1 1 1) orientation. The sample was exposed to air after the growth, and an annealing program under X-ray control was applied prior to the actual experiment to clean the sample surface. Thereby, the sample was heated to 920 K in vacuum to remove bulk oxide and several cycles of low pressure O_2 exposure at $T = 570$ K and subsequent annealing at $T = 920$ K were applied to remove carbon. Finally, the sample was exposed to 3×10^{-5} mbar of pure CO to remove residual chemisorbed oxygen and annealed to 920 K. As reported pre-

viously, this procedure leads to chemically clean, reactive particles with well-defined truncated octahedral shape [17,18], as depicted in Fig. 1(a). From the anisotropic broadening of the Pd Bragg reflections in different reciprocal space directions the average particle height after the sample cleaning procedure is determined to be 6 nm and their average diameter is 9 nm [13,18].

During the in situ X-ray diffraction experiments the sample was investigated under exposure to pure oxygen, pure CO, and oxygen/CO 1:1 mixtures close to 100 mbar total initial pressure at a controlled temperature of 570 K. From previous experiments it is known that PdO grows during the oxidation of Pd on MgO(0 0 1) in epitaxial relationship to the MgO substrate with 5 different domains (see Fig. 2(b)) [13]. Two of the domains have their c axis in the surface plane and a axis perpendicular to the surface (note, that PdO exhibits a tetragonal structure with $a = 330$ pm and $c = 520$ pm [13,19,20]). Their formation is monitored by angular θ scans with fixed momentum transfer at the PdO(1 0 3) Bragg reflection, during which the sample is rotated around its surface normal. During exposure to pure CO above 10^{-4} mbar the X-ray beam was switched off to avoid beam induced CO dissociation. The evolution of the sample structure under the varying chemical environment was followed by different reciprocal space scans as depicted in Fig. 1(c). Radial scans along H through the MgO(2 0 0) and Pd(2 0 0) Bragg reflections provide information on structural changes of the epitaxial Pd nanoparticles.

First, we turn to the results obtained in pure oxygen environment: oxygen was dosed stepwise with pressures starting from 1×10^{-6} mbar. The subsequent H and θ scans with increasing oxygen pressure are plotted in Fig. 2(a). Between 10^{-6} mbar and 10^{-2} mbar O_2 pressure, only a slight change of the Pd(2 0 0) signal is present, inline with a slight shape change of the particles [13]. At a pressure of 1×10^{-1} mbar, the formation of epitaxial PdO is observed, as inferred from the θ scan plotted in the lower part of Fig. 2(a). After raising the pressure further to 1 mbar, a strong increase of the signal of epitaxial PdO is recorded in addition to an increased background which points to the formation of polycrystalline PdO domains with no preferential angular in-plane orientation (Fig. 2(a), lower part). The Pd(2 0 0) signal is significantly diminished and the Bragg peak gets broadened inline with a shrinkage of the Pd nanoparticles. Such an oxidation behavior is according to our size dependent oxidation study of Pd/MgO(0 0 1) [18]. For particles with average diameter smaller than 9 nm the oxidation takes place via particle shrinkage and the formation of epitaxial PdO on the MgO surface, whereas for larger particles the formation of polycrystalline PdO on the particle facets is present.

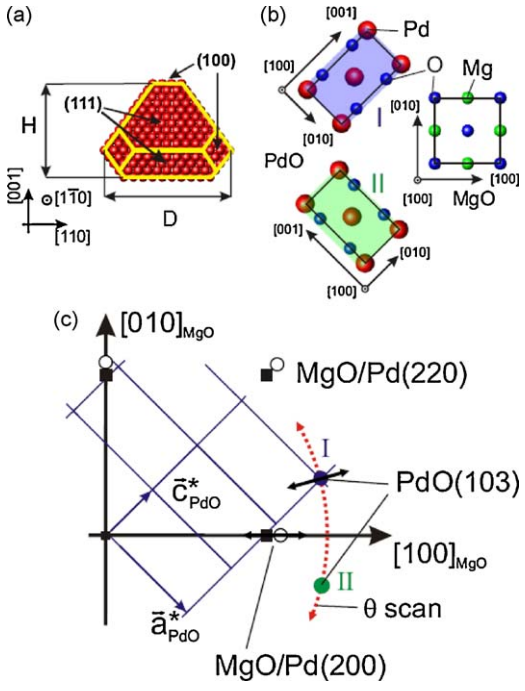

Fig. 1. (a) Truncated octahedral shape of Pd nanoparticles on MgO(0 0 1). In the present experiment the average particle height was $H = 6$ nm and the particle diameter $D = 9$ nm. (b) Two (out of five) epitaxial PdO domains observed on MgO(0 0 1) during Pd nanoparticle oxidation [13]. (c) Sketch of the in-plane reciprocal space ($L = 0$) investigated during the in situ X-ray studies. Squares (open circles) denote positions of MgO (Pd) Bragg reflections. The PdO reciprocal lattice for oxide domain I is included. The PdO(1 0 3) reflection is monitored for both domains during the in situ X-ray experiment by θ scans.

Subsequently, the sample was exposed to CO at 570 K; the corresponding X-ray scans are plotted in Fig. 2(b). At 10^{-5} mbar CO pressure the oxide reduction was observed to start and the Pd(2 0 0) reflection increases, which is explained straight forward by the re-growth of epitaxial Pd nanoparticles (Fig. 2(b), lower part). At 10^{-2} mbar CO pressure, the corresponding θ scan indicates the complete reduction of PdO by CO oxidation to CO_2 (Fig. 2(b), lower part). We note that at this pressure, the Pd(2 0 0) Bragg peak signal saturates below the value before the initial oxidation cycle, which may be related to the formation of differently oriented Pd islands.

During the third treatment, the sample was exposed to 50 mbar CO first (without X-ray exposure) and subsequently O_2 was introduced until a total pressure of 100 mbar was reached, which took about 20 s. Fig. 2(c) gives an overview of the corresponding X-ray scans during CO oxidation. We observed that the Pd(2 0 0) signal decreased during the reaction over 800 s and poorly ordered, epitaxial and randomly oriented PdO islands formed, as inferred from Fig. 2(c), bottom. The corresponding radial scan (Fig. 2(d)) confirms the formation of PdO. From the width of the PdO(1 0 3) reflection a PdO particle size of 3 nm can be estimated. At the same time, we find that a broad signal close to the MgO(2 0 0) reflection grows significantly during prolonged CO oxidation and CO_2 production (see Fig. 2(c), upper part, indicated by the upward arrow). During the reaction, the pressure inside the chamber decreased to 84 mbar, close to the theoretical value of 75 mbar. The deviation from the theoretical value is very likely related to a partial reaction taking place during the backfilling of the chamber with oxygen. The CO_2 production was in addition monitored by a mass spectrometer, which was connected to the chamber by a leak valve.

Further reciprocal space mapping revealed that the new phase which is formed during CO_2 production, is epitaxial to the MgO substrate and exhibits a lattice parameter close to MgO and a face centered cubic (fcc) structure.

To gain more insight into the structure and chemical activity of the new phase, the sample was annealed to 940 K for 10 min and it was subsequently oxidized at 770 K and 500 mbar O_2. During the annealing procedure PdO was decomposed, but the new phase persisted the heat treatment. During the final oxidation treatment, the remaining Pd nanoparticles were fully converted into PdO, whereas the new phase also survived the harsh oxidation conditions.

4. Post-experimental structural and chemical characterization

After the final oxidation step at 940 K and 500 mbar O_2, different parts of the sample were characterized ex situ using a combination of transmission electron microscopy and different spectroscopy techniques, as described in this section.

4.1. TEM analysis

To shed more light onto the structure and composition of the new phase formed during CO_2 production, cross-sectional TEM

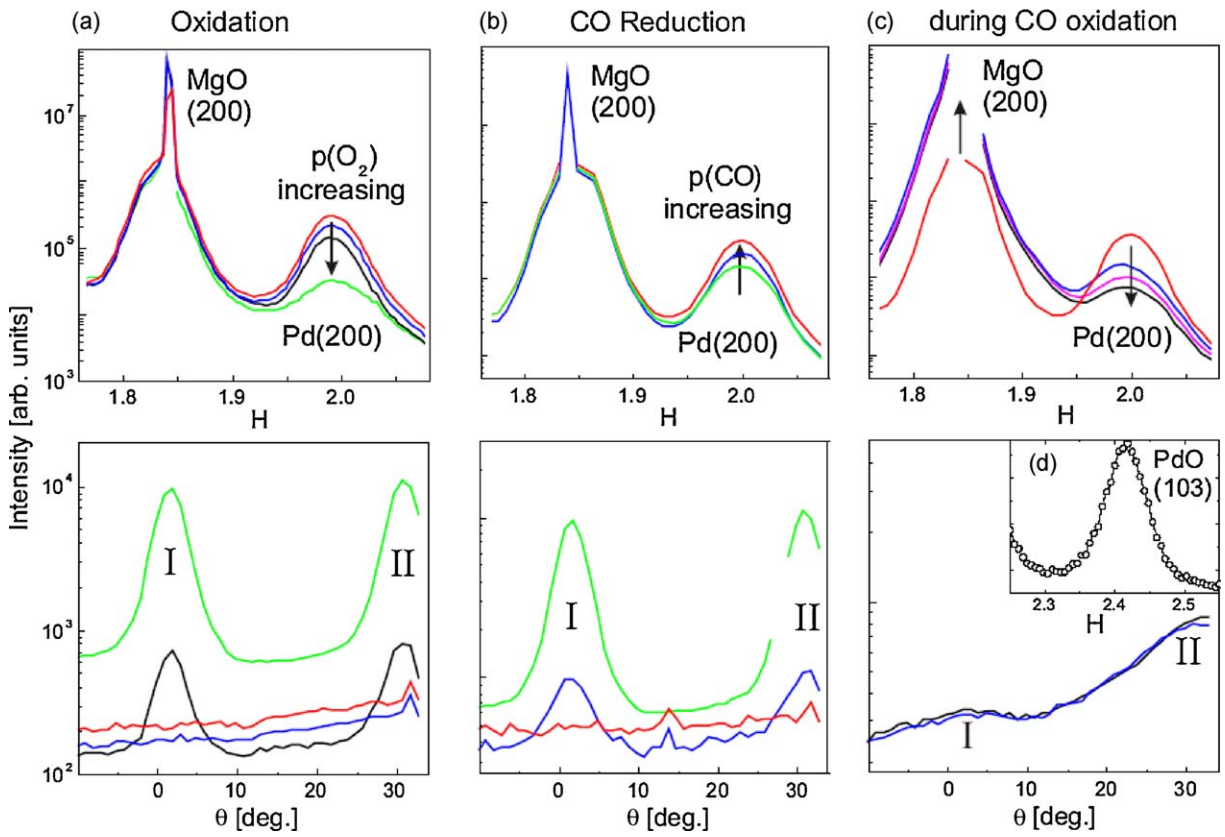

Fig. 2. (a)–(c): Upper part: H scan through the MgO(2 0 0) and the Pd(2 0 0) Bragg reflection, lower part: θ scan with fixed momentum transfer at the PdO(1 0 3) Bragg reflection; peaks arising from domains I and II are labeled. (a) Scans during increasing oxygen pressure: 10^{-4} mbar (red lines), 10^{-2} mbar (blue lines), 10^{-1} mbar (black lines), 1 mbar (green lines) (b) scans during CO reduction: oxidized sample in vacuum (green lines), 10^{-5} mbar (blue lines), 10^{-2} mbar (red lines) (c) scans during CO oxidation reaction (initial mixture 50 mbar O_2/50 mbar CO) after reduction in vacuum (red curves), H scans: 150 s (blue curve), 330 s (magenta curve), 800 s (black curve), θ scans: 500 s (blue curve), 960 s (black curve) after starting the CO oxidation reaction. Times refer in the first case to the measurement of the Pd(2 0 0) reflection and in the second case to the reflection of domain I. (d) radial scan across the Pd(1 0 3) reflection from domain I (after 630 s). (For interpretation of the references to colour in this figure legend, the reader is referred to the web version of the article.)

specimens were prepared for TEM imaging and analytical studies. Fig. 3(a) and (b) show different regions of the sample. In Fig. 3(a) uncovered, oxidized Pd particles are resolved residing on the MgO substrate. As can be observed from additional TEM images on varying positions of the sample, there exist also areas which are covered by a ≈100 nm thick layer (see Fig. 3(b)). This inhomogeneity of the sample surface is also confirmed by scanning electron microscopy (not shown here). At the interface to the substrate, nanoparticles are visible, which are covered by the thick overlayer. The diffraction pattern from this part of the sample (including overlayer, nanoparticles and the substrate, shown in Fig. 3(c)) exhibits diffraction spots compatible with MgO in the (0 1 0) azimuth and powder rings also corresponding to lattice spacings close to values for MgO (note, that diffraction patters from the overlayer region show powder rings only). This implies that the nanoparticles at the interface exhibit lattice spacings close to the MgO substrate values. In addition, on both images a disturbed zone of 15 nm thickness in the MgO substrate can be identified at the interface. Fig. 3(a) shows, that this interfacial MgO consists of small crystallites with diameters of 2–10 nm and heights of a few nm.

4.2. EDXS and EELS analysis

The chemical analysis was performed on a region of the specimen covered with the unknown overlayer. Fig. 4(a) shows a high-angle annular dark field (HAADF) STEM image of the investigated sample region exhibiting a strong material contrast for the nanoparticles. Four regions of the sample, as labeled in Fig. 3(b) and Fig. 4(a), namely the MgO bulk (I), the small MgO crystallites (II), the interfacial particles (III) and the covering layer (IV) were analyzed. The EDX spectra displayed in Fig. 4(b) show significant contributions of magnesium, palladium, oxygen, argon and carbon. Most important, a pronounced magnesium and oxygen signal can be detected in the overlayer (IV), but no Pd signal. The carbon signal observed at all positions of the sample does not allow drawing any conclusions, because the TEM specimen was carbon coated to avoid sample charging. The argon signal is an artifact of the argon ion-milling process during TEM sample preparation. A Pd signal can be found only at the position of the particles (region (III)). Both, oxygen and magnesium signals are much weaker in the region of the particles, but their ratio is similar to region (IV), where the overlayer is present. This is inline with an overgrowth of the particles by the material that can also be observed in region (IV). In region (II) and (I) finally magnesium and oxygen signals are detected as expected for pure MgO. The chemical composition of the different sample regions (I)–(IV) is confirmed by EELS measurements performed in the same apparatus simultaneously with the EDX measurements, as plotted in Fig. 4(c).

4.3. AES sputter profiling

AES sputter-depth profiling was performed to clarify the role of carbon in the formation of the Mg and O containing overlayer (see Section 2). Fig. 5(a) shows the thus obtained concentration-depth profiles of C, Pd, O and Mg up to an effective sputter depth of about 600 nm. The compositional changes with sputter depth can be roughly subdivided into four different regions, labeled 1–4. All elements are present before sputtering. The outer surface

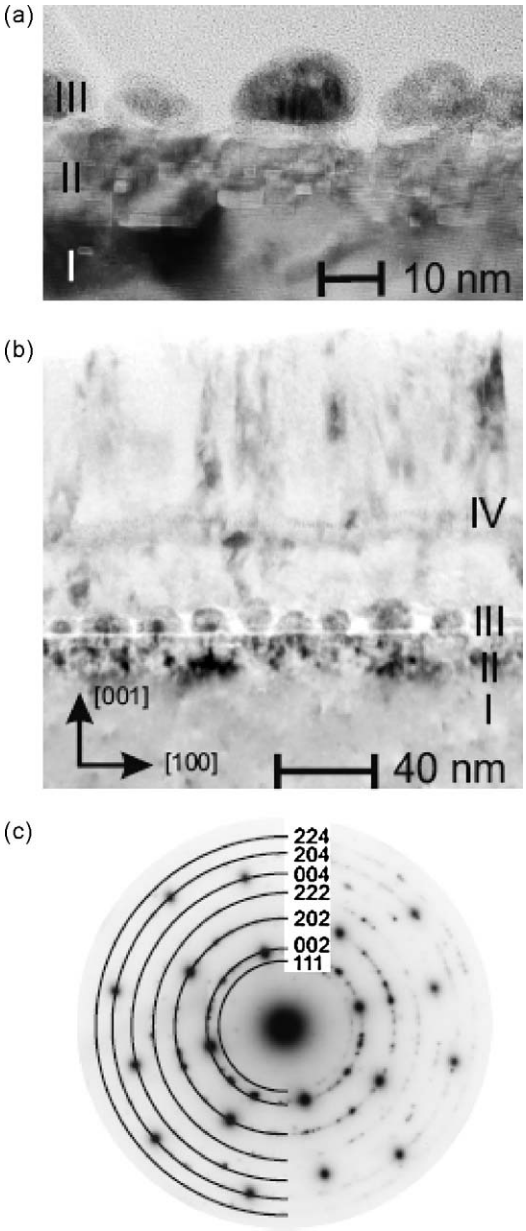

Fig. 3. Bright field images of cross-sectional TEM specimens along the [0 1 0] direction in a sample region without (a) and with overlayer (b). Regions I–IV label the MgO substrate, a disturbed substrate region close to the interface, the nanoparticle region and the overlayer, respectively. (c) Electron diffraction pattern of the sample region shown in (b), data (left), simulated diffraction pattern (right). All diffraction spots can be explained by MgO lattice spacings.

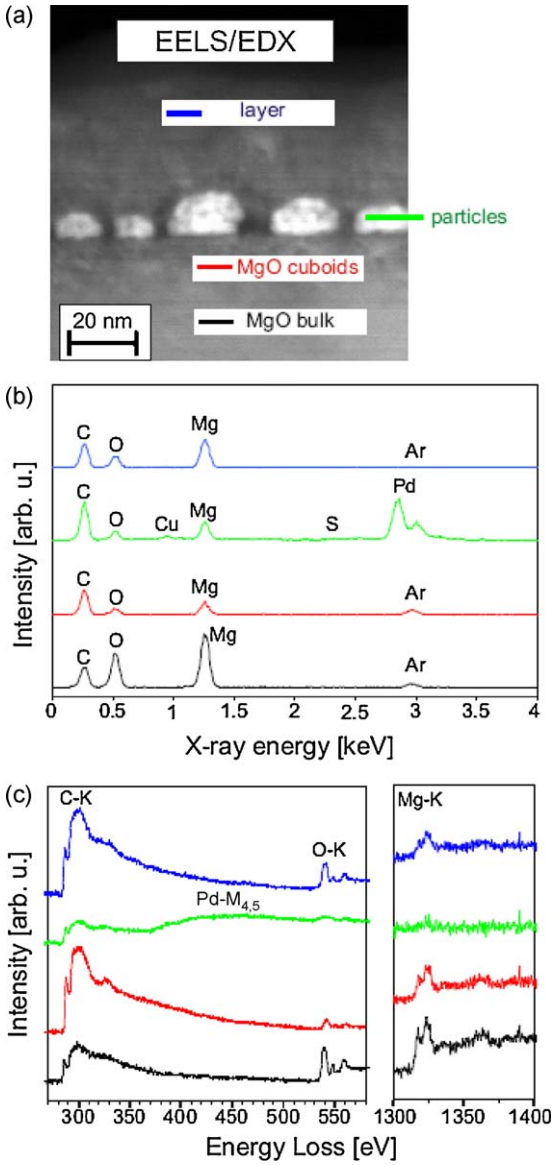

Fig. 4. (a) Cross-section image obtained in the STEM, defining the regions used for the chemical analysis. (b and c) EDX (EELS) spectra of the different sample regions. For details, see text.

(designated as region 1) is associated with a very thin surface layer enriched in C. In region 2, the C signal gradually decreases, while the corresponding Pd, O and Mg signals slightly increase, with increasing sputter depth. Both results give evidence that the Mg and O containing layer identified by EDXS and EELS (see above) also contains a considerable amount of carbon. The detection of Pd in region 2 can be attributed to the inhomogeneous coverage of the surface with the Mg–O–C layer (i.e. the AES analysis only probes the laterally averaged surface composition). In region 3, both the C and Pd concentrations decrease with increasing sputter depth, which indicates that both the Mg–O–C layer segments and the Pd particles get sputtered away. Finally, at the transition from region 3 to 4, the Mg and O concentrations strongly increase, while the C and Pd decrease, with increasing sputter depth. This marks the

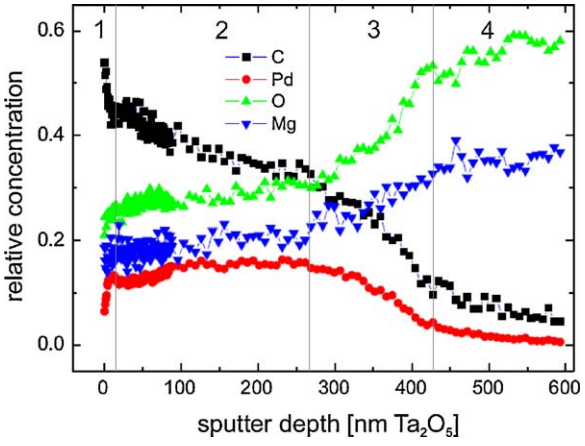

Fig. 5. C, Pd, O and Mg relative concentration as a function of the depth obtained by AES sputter depth profiling.

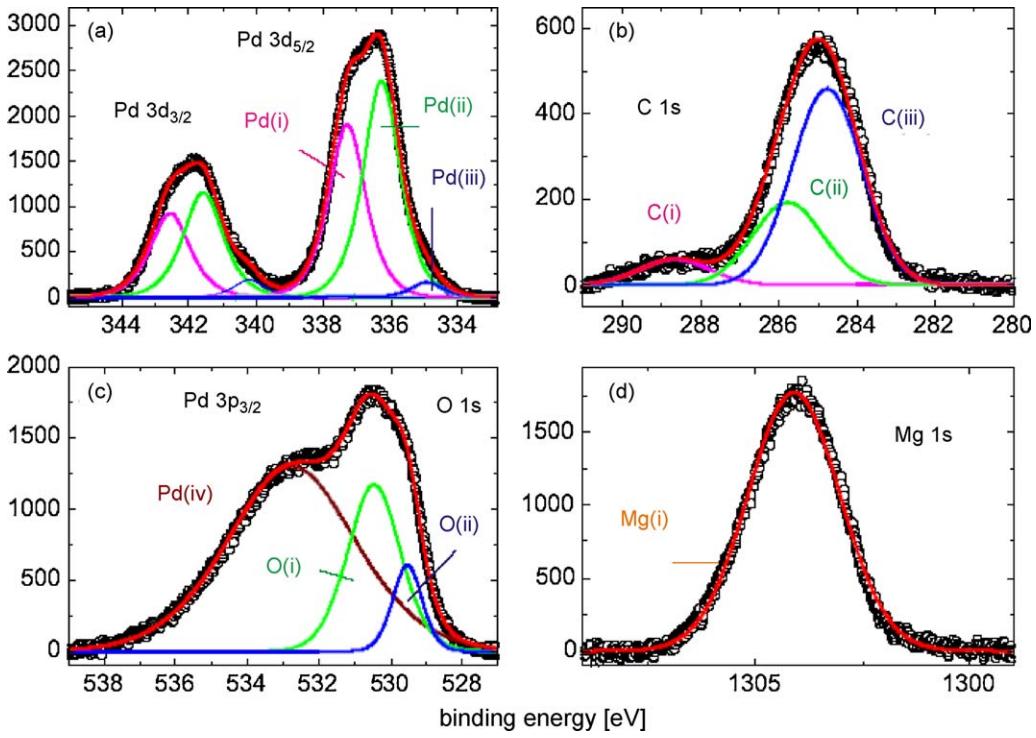

Fig. 6. Reconstruction of the (a) metallic and oxidic Pd $3d_{5/2}$ main peaks, (b) the C 1s main peaks, (c) the combined Pd $3p_{3/2}$ and O 1s main peaks, and (d) the oxidic Mg 1s main peak from the measured XPS spectra (after Shirley-type background subtraction), as recorded from the Pd/MgO(1 0 0) sample after several cycles of CO oxidation and final oxidation. See text and Section 2 for details.

interface to the MgO substrate, where the Mg and O concentrations gradually approach constant values and the C and Pd concentrations become negligible (region 4).

4.4. XPS results

XPS analysis of the sample surface after the X-ray experiment shows that the surface is constituted of Mg, C, O and Pd, in agreement with the AES results. The different local chemical states of the elements were identified by reconstruction of the measured C 1s, Pd $3d_{3/2}$, Pd $3d_{5/2}$, O 1s, Pd $3p_{3/2}$ and Mg 1s XPS spectra [see Fig. 6(a)–(d)]. The binding energies (BE) of the thus resolved peak components, as well as their chemical assignment (see below), are reported in Table 1. It follows that the Pd $3d_{5/2-3/2}$ spectrum could be accurately fitted (while maintaining the spin-orbit splitting of 5.3 eV) with three different chemical species, designated as Pd(i), P(ii) and Pd(iii) [see Fig. 6(a)]. The weak Pd(iii) main peak at 334.9 eV can be assigned to some residual metallic Pd [19], which survived the final oxidation of the sample and did not give rise to a Bragg like X-ray diffraction signal after the final oxidation. The Pd(ii) main peak at 336.3 eV corresponds well to bulk PdO [21]. The additional Pd(i) main peak at 337.3 eV can be attributed to the formation of a Pd oxide in a higher oxidation state, such as PdO_2. Its formation was put forward by a recent density functional theory study [22], and it is compatible with the oxidation conditions applied in our experiment. The formation of Pd–C compounds accessible to XPS can be excluded, because it gives rise to a Pd $3d_{5/2}$ component shifted by approximately 0.6 eV to higher BE side of the Pd(i) peak [23], which is not observed here. The corresponding C 1s spectrum [see Fig. 6(b)] is accurately described by three spectral components. The C(ii) and C(iii) main peaks at 285.8 eV and 284.8 eV can be attributed to CO and adventitious carbon, respectively, in accordance with the observation of a carbon rich layer at the outer sample surface by AES sputter profiling. The weak C(i) main peak at a relatively high BE of 288.7 eV, on the other hand, points to the formation of a carbonate species [24–26] (note: the C(i) signal intensity is attenuated by the C-enrichment at the outer sample surface; see above).[1] The spectral reconstruction of the Pd $3p_{3/2}$–O 1s region is shown in Fig. 6(c); the intrinsically very broad Pd $3p_{3/2}$ peak at 532.8 eV, as well as the corresponding O 1s main peak at around 529.5 eV (designated as O(ii)) are characteristic for PdO [21]. The predominant O 1s main peak at 530.5 eV (designated as O(i)) complies well with the O 1s peak component arising from the Mg–C–O-containing surface layer, designated as $MgCO_3$, as formed after CO_2 attack on MgO powder in Ref. [24] (see footnote 1). The corresponding Mg 1s main peak at 1304.1 eV (Fig. 6(d)) also matches very well with the corresponding Mg 1s

Table 1
Binding energies and chemical assignment of the resolved Pd $3d_{5/2}$, C 1s, Pd $3p_{3/2}$, O 1s and Mg 1s peak from the measured XPS spectra pertaining to Fig. 6. The Mg carbonate phase is designated in the chemical assignment as '$MgCO_3$'-like. See text for further details.

Core-level	Main peak	Binding energy (eV)	Chemical assignment
Pd $3d_{5/2}$	Pd(i)	337.3	PdO_2
	Pd(ii)	336.3	PdO
	Pd(iii)	334.9	Metallic Pd
Pd $3p_{3/2}$	Pd(iv)	532.8	PdO/PdO_2
O1s	O(i)	530.5	$MgCO_3$-like
	O(ii)	529.5	PdO
Mg 1s	Mg(i)	1304.1	$MgCO_3$-like
C 1s	C(i)	288.7	$MgCO_3$-like
	C(ii)	285.8	CO
	C(iii)	284.8	Adventitious C

[1] For comparison with the BE values of the resolved C 1s, O 1s and Mg 1s main peaks in the present study, all corresponding BE values in Ref. [24] were shifted by +4.88 eV to correct for the obvious overcompensation of differential charging by the employed floodgun in Ref. [24].

peak for MgO powder attacked by CO_2 (see Ref. [24] and footnote 1). To summarize, XPS gives clear evidence for a coexistence of PdO and a phase containing Mg, O, C at the surface of the sample.

5. Discussion

The results described in the last section obtained by ex situ structural and chemical probes give evidence that after the CO oxidation experiment and final oxidation our model catalyst system Pd/MgO(1 0 0) has transformed into a Mg, C and O containing layer and PdO, laterally coexisting on the surface. At the surface, XPS reveals the presence of a carbonate species, which is reported to be stable up to 1000 K [25], explaining why it could not be removed during the in situ X-ray experiment (maximum annealing temperature 940 K). Moreover, the observation of Mg carbonate formation is inline with a recent in situ Fourier transform infrared spectroscopy study on Pd/MgO under CO oxidation conditions [27]. The question arises how the ex situ results can be connected to the in situ X-ray experiments described in Section 3 and what can be learned on the detailed mechanism taking place during the apparent deactivation of the model catalyst.

The most prominent observations from the in situ X-ray experiments during CO oxidation are the decrease of the Pd signal stemming from epitaxial Pd nanoparticles with Pd bulk lattice spacing and the formation of a new broad reflection close to the MgO(2 0 0) substrate with increasing intensity during the reaction. On the other hand, from the TEM of the cross-section and the EDX/EELS results it is evident, that Pd containing nanoparticles are present below the Mg–C–O layer at the interface to the MgO substrate, which are deactivated because of the growth of the layer. In addition, the selected area diffraction containing the Mg–C–O layer, the nanoparticles below the layer and the MgO substrate shows only diffraction spots and Debye–Scherrer rings compatible with MgO lattice spacings (with the Debye–Scherrer rings stemming from the overlayer only). We therefore conclude that the overlayer mainly consists of polycrystalline MgO embedded in a carbon bearing network. This conclusion is also supported by the EDX/EELS O/Mg intensity ratios, which are comparable for the overlayer and the MgO substrate. Crystalline $MgCO_3$ has a corundum structure [28] with *d*-spacings different from MgO and should be visible in the TEM diffraction pattern. In addition, the combined X-ray and TEM findings are compatible with the formation of Pd nanoparticles with a lattice constant close to the value of the MgO substrate.

The expansion of the Pd nanoparticle lattice spacing can be attributed to the incorporation of carbon atoms, occupying interstitial octahedral sites [1,29]. Note that thermal expansion of Pd cannot account for this effect. The formation of atomic carbon is promoted by the disproportionation reaction: $2CO \rightarrow CO_2 + C$, which may take place on Pd nanoparticles during CO oxidation [27,30]. Although molecular beam experiments showed that for a 1:1 CO/O_2 mixture the surface of Pd nanoparticles should be in an oxygen-rich state at 570 K [31], apparently enough CO adsorbs under high-pressure conditions, which undergoes dissociation providing atomic carbon that is dissolved into the Pd nanoparticles.

Fig. 7(a) and (b) are summarizing the proposed scenario: O_2 and CO adsorb dissociatively on Pd nanoparticles, CO_2 is either produced by CO disproportionation or by direct reaction with adsorbed oxygen species. The resulting CO_2 molecules can either desorb or spill-over onto the MgO substrate, where they react to form the Mg–O–C layer. The reaction with the MgO substrate may be responsible for the formation of the defect rich zone at the interface as observed in the TEM of the cross-section. Grain boundaries and point defects may act as diffusion channels during further carbon incorporation.

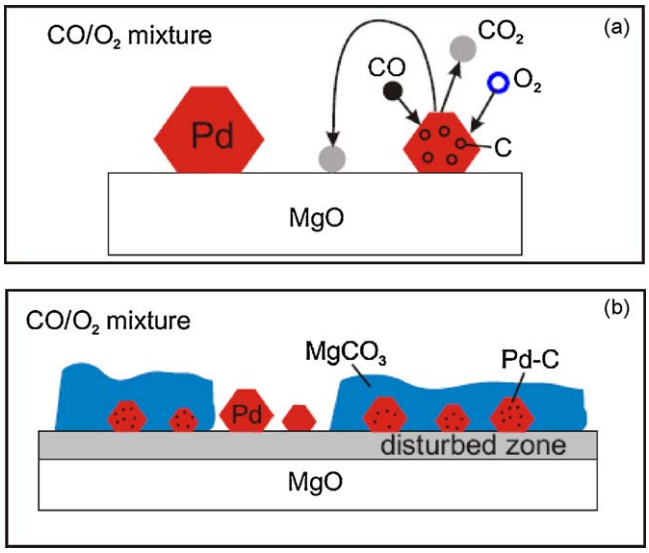

Fig. 7. Proposed scenario of CO oxidation and deactivation over a Pd/MgO(1 0 0) model catalyst. (a) CO and O_2 dissociate on the Pd nanoparticle surface, remaining carbon is dissolves into the Pd lattice, produced CO_2 spills over onto the MgO substrate, where it reacts with magnesium. (b) Continuous deactivation of the Pd nanoparticles by overgrowth of a Mg–O–C containing layer.

6. Conclusion

In conclusion, we have shown that the model catalyst Pd/MgO(0 0 1) can be cycled between Pd oxide and metallic Pd by oxidation and CO reduction at 570 K. During CO exposure and CO oxidation in a 1:1 CO/O_2 mixture at a total pressure of 100 mbar and 570 K, Pd nanoparticles incorporate carbon atoms, allowing them to expand and to accommodate to the MgO substrate lattice spacing. We observe the formation of poorly ordered PdO during CO oxidation, which might be located either on the MgO support or on the Pd nanoparticle facets. Our data do not allow drawing any conclusion to which extent disordered PdO is involved in the CO oxidation reaction or metallic Pd nanoparticles. Finally, a CO_2 spill-over mediated deactivation of the model catalyst system takes place via the formation of a layer containing MgO nanocrystallites in a carbon bearing network and a surface carbonate layer. Our results underline the importance to study model catalyst systems composed of metal or oxide nanoparticles with well defined shape on ordered oxide supports at ambient conditions, since new reaction pathways may be opened at elevated pressures.

Acknowledgements

The authors thank M. Kelsch and U. Salzberger for the TEM specimen preparation. P. Kopold and B. Siegle are acknowledged for TEM and AES sputter profile measurements. The European Union is acknowledged for financial support under contract no. NMP3-CT-2003-505670 (NANO2).

References

[1] D. Teschner, J. Borsodi, A. Wootsch, Z. Révay, M. Hävecker, A. Knop-Gericke, S.D. Jackson, R. Schlögl, Science 320 (2008) 86.
[2] A.K. Datye, J. Bravo, T.R. Nelson, P. Atanasova, M. Lyubovsky, L. Pfefferle, Appl. Catal. A: Gen. 198 (2000) 179.
[3] E. Lundgren, A. Mikkelsen, J.N. Andersen, G. Kresse, M. Schmid, P. Varga, J. Phys. Condens. Matter 18 (2006) R481.
[4] C.H.F. Peden, D.W. Goodman, D.S. Blair, P.J. Berlowitz, G.B. Fisher, S.H. Oh, J. Phys. Chem. 92 (1988) 1563.
[5] P.J. Berlowitz, C.H.F. Peden, D.W. Goodman, J. Phys. Chem. 92 (1988) 5213.
[6] P. Mars, D.W. van Krevelen, Chem. Eng. Sci. 3 (1954) 41.

[7] B.L.M. Hendriksen, S.C. Bobaru, J.W.M. Frenken, Surf. Sci. 552 (2004) 229.
[8] B.L.M. Hendriksen, S.C. Bobaru, J.W.M. Frenken, Catal. Today 105 (2005) 234.
[9] M. D. Ackermann, PhD thesis, Leiden, 2007.
[10] J. Rogal, K. Reuter, M. Scheffler, Phys. Rev. Lett. 98 (2007) 046101.
[11] T. Schalow, B. Brandt, M. Laurin, S. Schauermann, J. Libuda, H.-J. Freund, J. Catal. 242 (2006) 58.
[12] B. Brandt, T. Schalow, M. Laurin, S. Schauermann, J. Libuda, H.-J. Freund, J. Phys. Chem. C 111 (2007) 938.
[13] N. Kasper, A. Stierle, P. Nolte, Y. Jin-Phillipp, T. Wagner, D.G. de Oteyza, H. Dosch, Surf. Sci. 600 (2006) 2860.
[14] P. Bernard, K. Peters, J. Alvarez, S. Ferrer, Rev. Sci. Instr. 70 (1999) 1478.
[15] A. Strecker, U. Salzberger, J. Mayer, Prakt. Metallogr. 30 (1993) 482.
[16] S. Hoffmann, Surf. Interface Anal. 35 (2003) 556.
[17] C.R. Henry, Surf. Sci. Rep. 31 (1998) 231.
[18] P. Nolte, A. Stierle, N. Kasper, N.Y. Jin-Phillipp, H. Reichert, A. Rühm, J. Okasinski, H. Dosch, Phys. Rev. B 77 (2008) 115444.
[19] J. Waser, H.A. Levy, S.W. Peterson, Acta Cryst. 6 (1953) 661.
[20] A. Stierle, N. Kasper, H. Dosch, E. Lundgren, J. Gustafson, A. Mikkelsen, J.N. Andersen, J. Chem. Phys. 122 (2005) 044706.
[21] G. Ketteler, D.F. Ogletree, H. Bluhm, H. Liu, E.L.D. Hebenstreit, M. Salmeron, J. Am. Chem. Soc. 127 (2005) 18269.
[22] A. Dianat, N. Seriani, M. Bobeth, W. Pompe, L.C. Ciacchi, J. Phys. Chem. C 112 (2008) 13623.
[23] D. Teschner, E. Vass, M. Hävecker, S. Zafeiratos, P. Schnörch, H. Sauer, A. Knop-Gericke, R. Schlögl, M. Chamam, A. Wootsch, A.S. Canning, J.J. Gamman, S.D. Jackson, J. McGregor, L.F. Gladden, J. Catal. 242 (2006) 26.
[24] B.V. Christ, Handbook of Monochromatic XPS Spectra, vol. 1, XPS International LLC, Mountain View, 2004.
[25] D.K. Aswal, K.P. Muthe, S. Tawde, S. Chodhury, N. Bagkar, A. Singh, S.K. Gupta, J.V. Yakhmi, J. Cryst. Growth 236 (2002) 661.
[26] D.K. Aswal, K.P. Muthe, A. Singh, S. Sen, K. Shah, L.C. Gupta, S.K. Gupta, V.C. Sahni, Physica C 363 (2001) 2008.
[27] H. Borchert, B. Jürgens, V. Zielasek, G. Rupprechter, S. Giorgio, C.R. Henry, M. Bäumer, J. Catal. 247 (2007) 145.
[28] H. Effenberger, K. Mereiter, J. Zemann, Z. Krist. 156 (1981) 233.
[29] S.B. Ziemecki, G.A. Jones, D.G. Swartzfager, R.L. Harlow, J. Faber Jr., J. Am. Chem. Soc. 107 (1985) 4547.
[30] G. Rupprechter, V.V. Kaichev, H. Unterhalt, M. Morkel, V.I. Bukhtiyarov, Appl. Surf. Sci. 235 (2004) 26.
[31] V. Johanek, M. Laurin, A.W. Grant, B. Kasemo, C.R. Henry, J. Libuda, Science 304 (2004) 1639.